# Cost-Effective High-Performance Charge-Carrier-Transport-Layer-Free Perovskite Solar Cells Achieved by Suppressing Ion Migration

Tao Ye<sup>1</sup>\*, Yuchen Hou<sup>1</sup>, Amin Nozariasbmarz<sup>1</sup>, Dong Yang<sup>1</sup>, Jungjin Yoon<sup>1</sup>, Luyao Zheng<sup>1</sup>, Ke Wang<sup>2</sup>, Kai Wang<sup>1</sup>\*, Seeram Ramakrishna<sup>3</sup>, Shashank Priya<sup>1,2</sup>\*

<sup>1</sup>Department of Materials Science and Engineering, Pennsylvania State University, University Park, Pennsylvania 16802, United States

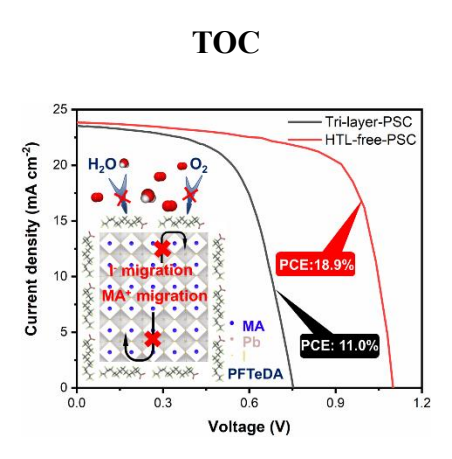
<sup>2</sup>Materials Research Institute, Pennsylvania State University, University Park, Pennsylvania 16802, United States

<sup>3</sup>Centre for Nanofibers and Nanotechnology, National University of Singapore, Singapore 117576, Singapore

### Abstract

Perovskite solar cells (PSCs) without charge-carrier-transport-layers (CTLs) are theoretically achievable due to the ambipolar charge carrier transfer characteristics presenting in perovskites. However, the power conversion efficiency (PCE) of the CTL-free PSCs needs further improvement. Herein, we provide breakthrough in the fabrication of the cost-effective high-performance hole transport layer (HTL) free PSC and tri-layer-PSC with device configurations of fluorine doped tin oxide (FTO)/SnO<sub>2</sub>/perovskite/carbon and FTO/perovskite/carbon, respectively. we introduce

perfluorotetradecanoic acid (PFTeDA) with a carbonyl unit and carbon fluorine bonds to suppress the ion migration and reduce the crystal defects in perovskites. The modified carbon-based HTL-free-PSC shows a record PCE of 18.9%. Furthermore, the PFTeDA molecules are found existing at the grain boundaries between the perovskite crystals, resulting in enhanced environmental, thermal, and light stabilities for the resultant cost-effective high-performance CTL-free PSCs.



Intensive efforts have been made to enhance the sunlight-to-electricity power conversion efficiency (PCE) of perovskite solar cells (PSCs), including optimization of perovskite precursor composition, <sup>1,2</sup> quality improvement of the perovskite film, <sup>3,4</sup> and development of the functional charge transfer layers<sup>5,6</sup>. These efforts have led to increase in PCE of PSCs from 3.8% to a certified value of above 25%. <sup>7-13</sup> The state-of-the-art PSCs are constructed using a layer-by-layer deposition approach with multiple buffering layers. The PSC structure comprises of the perovskite light absorber which is sandwiched between electron transport layer (ETL) and hole transport layer (HTL). This sandwich structure is further capped by a metal electrode deposited using vacuum-

thermal evaporation. There are several physical and structural requirements in designing this complex multi-layer-structure, which demands not only continuous material innovation but also manufacturing process development. 14-17 Multiple factors will raise both transition and scaling challenges for PSC fabrication, including the raw material cost for chemicals such as 2,2',7,7'-Tetrakis[N,N-di(4-methoxyphenyl)amino]-9,9'-spirobifluorene (spiro-OMeTAD), polytriarylamine (PTAA), and phenyl C<sub>61</sub> butyric acid methyl ester (PCBM), and complex processing of various buffer layers and metal electrodes (such as high temperature sintering of TiO2, or thermal evaporation of Au, Ag, Al, or C<sub>60</sub>). To address these challenges, here, we take a radical approach in design of PSCs. Can we design an HTL-free structure with low temperature processed SnO<sub>2</sub> as ETL and carbon as back electrode (fluorine doped tin oxide (FTO)/SnO<sub>2</sub>/perovskite/carbon), to substantially lower the cost? Or even extend further to a simplified tri-layer device structure in the form of FTO/perovskite/carbon? Both types of PSCs will have transformative impact in the advancement of solar cell technology by decreasing the usage of chemicals and reducing manufacturing cost and steps.

Previous valuable results have shown that the perovskite materials exhibit excellent optoelectrical properties, such as high absorption coefficients, <sup>18,19</sup> fast exciton dissociation, <sup>20,21</sup> ambipolar carrier transport, <sup>22,23</sup> and long charge carrier diffusion lengths <sup>24,25</sup>. Due to the low exciton binding energy, the photogenerated excitons in perovskite can be spontaneously dissociated into free electrons and holes at room

temperature (RT) without the assistance of charge-carrier-transport-layers (CTLs). Also, perovskite with small effective mass of electrons and hole is a good transport medium for electronic charge carriers, high defect-tolerance, good ambipolar charge carrier transport, and long charge carrier diffusion length. Furthermore, interfacial effect such as band bending at the perovskite/electrode interface has also been proposed as the underlying driving force for the charge extraction in prior reported HTL-free or ETL-free PSCs. 28-33

Counter electrodes in PSCs are usually deposited by thermal evaporation of metal sources (Al, Cu, Ag, and Au) under high vacuum (below 10<sup>-5</sup> Torr), which increases the fabrication complexity and overall cost. <sup>17,34</sup> More importantly, in abovementioned HTL-free-PSCs and tri-layer-PSCs, the direct metal/perovskite contact can induce severe migration of metal atoms from metal electrodes into underneath layers <sup>35,36</sup>, causing detrimental influence on the performance and long-term stability. Carbon materials, on the contrary, have been demonstrated as an easy processable and cost-effective electrode candidates, bearing a suitable work function of ~ -5.0 eV, which matches well with the valance band maximum of methylammonium lead halide (MAPbI<sub>3</sub>). <sup>3,5,17,34,37-39</sup> Although the successful fabrication of the HTL-free-PSCs and tri-layer-PSCs with low-cost carbon electrodes is a landmark event, PCE values of these devices need further improvement.

Herein, we demonstrate the construction of efficient MAPbI<sub>3</sub>-based HTL-free-PSCs

(FTO/SnO<sub>2</sub>/MAPbI<sub>3</sub>/carbon) and tri-layer-PSCs (FTO/MAPbI<sub>3</sub>/carbon) by suppressing the ion migration and reducing the crystal defects through perfluorotetradecanoic acid (PFTeDA) modification. The resultant HTL-free-PSC shows a record PCE of 18.9%. These modified devices exhibited minimized PCE variations when measured at different scan rates under simulated 1 Sun illumination. The PFTeDA addition is found to increase the stability of the perovskite crystals, leading to enhanced environmental, thermal, and light stabilities for the resultant PSCs.

MAPbI<sub>3</sub> is chosen as light absorber for PSC construction due to its remarkable ion migration characteristics and high-reproducibility.<sup>32,40,43</sup> The MA<sup>+</sup> and I<sup>-</sup> are recognized as the dominant positive and negative mobile ions in the MAPbI<sub>3</sub> system.<sup>40,43</sup> The possible migration pathways for MA<sup>+</sup> and I<sup>-</sup> can be Schottky defects, grain boundaries, and lattice distortions.<sup>40</sup> The densities of MA<sup>+</sup>/I<sup>-</sup> ions and the migration pathway can be simply tuned by changing the precursor ratio in the MAPbI<sub>3</sub> system. Thus, the PCE variations induced by ion migration within different types of MAPbI<sub>3</sub> devices can be easily tailored by tuning the ratio of MAI:PbI<sub>2</sub> in a small region (0.94-1.06, this specific MAI:PbI<sub>2</sub> molar ratio value is used here to represent the perovskite film deposited with this precursor).

The performance results of the PSCs are presented in Figure 1. First, the full devices with a configuration of FTO/SnO<sub>2</sub>/perovskite/spiro-OMeTAD/Au (briefly referred to as full-PSC) were fabricated. Figure 1a shows the photocurrent density voltage (*J-V*)

curves of the full-PSCs fabricated using different perovskite light absorbers. Measurements were conducted under simulated 1 Sun radiation with a scan rate of 1 V s<sup>-1</sup>. The PCE of the 0.94 based full-PSC was 19.3% with an open-circuit voltage ( $V_{oc}$ ) of 1.13 V, short-circuit current density ( $J_{sc}$ ) of 22.95 mA cm<sup>-2</sup>, and fill factor (FF) of 0.742. The PCE increased to 20.4% for the 1.00 based full-PSC with an  $V_{oc}$  of 1.13 V,  $J_{sc}$  of 23.62 mA cm<sup>-2</sup>, and FF of 0.761. The incident photon-to-electron conversion efficiency (IPCE) spectrum of the 1.00 based full-PSC is shown in Figure S1. The integrated current value was 23.24 mA cm<sup>-2</sup> for this device, which agrees closely with the  $J_{sc}$  value extracted from J-V characteristic. The PCE decreased to 18.6% for the 1.06 based full-PSC with a  $V_{oc}$  of 1.10 V,  $J_{sc}$  of 22.73 mA cm<sup>-2</sup>, and FF of 0.738. The detailed photovoltaic parameters for all the five groups of full-PSCs can be found in Table S1. These results agree with the PCE statistics for the five groups of full-PSCs, as shown in Figure 1b. Figure 1c shows the PCE variations measured at different scan rates (2 V  $s^{-1}$ , 1 V  $s^{-1}$ , 0.5 V  $s^{-1}$ , 0.1 V  $s^{-1}$ , and 0.05 V  $s^{-1}$ ) for the five groups of full-PSCs. The measured PCEs of 0.94, 1.03, and 1.06 based full-PSCs exhibited a slightly decreasing trend as the scan rate decreased from 2 V s<sup>-1</sup> to 0.05 V s<sup>-1</sup>. This trend was not significant for the 0.97 and 1.00 based full-PSCs.

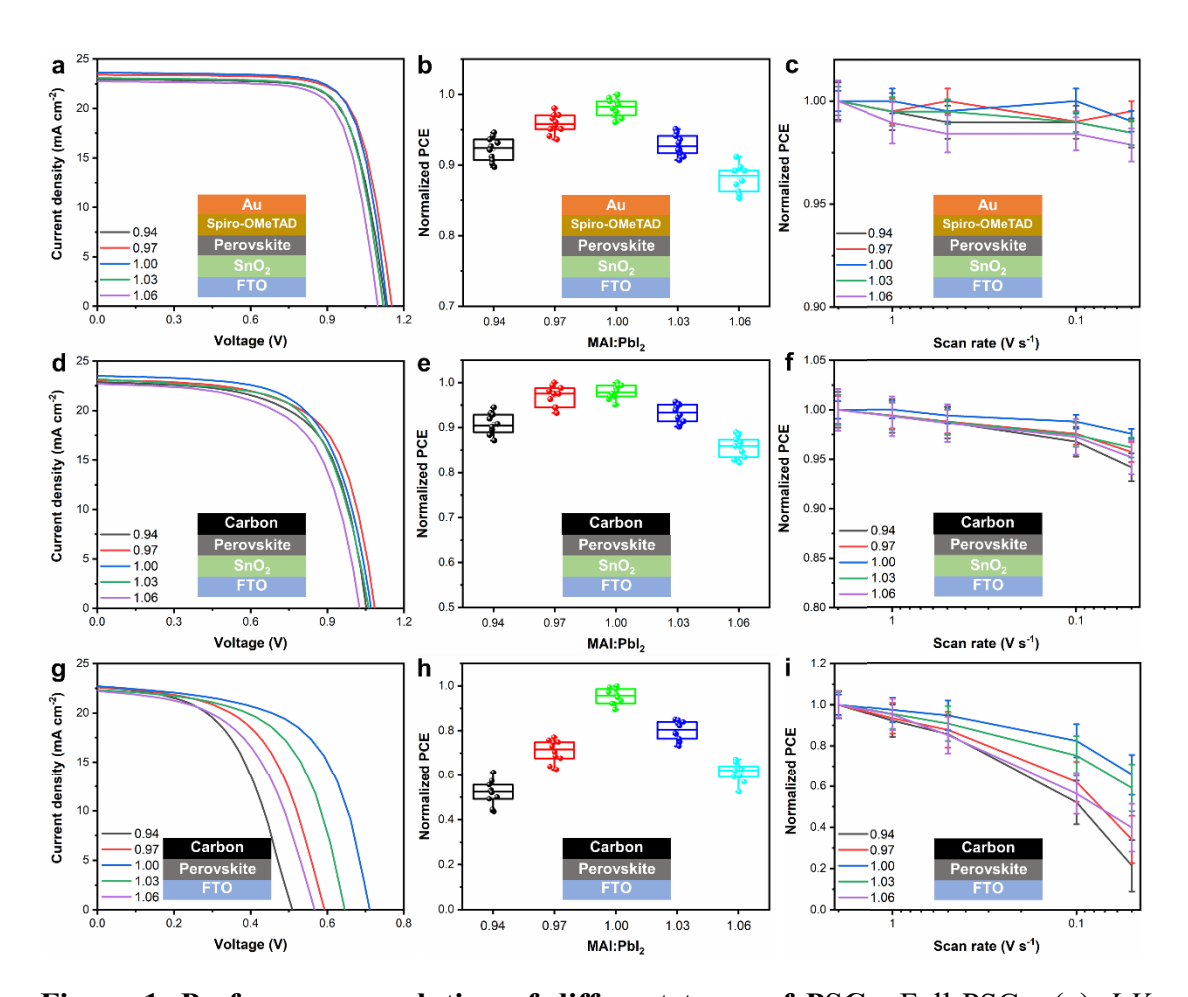


Figure 1. Performance evolution of different types of PSCs. Full-PSCs: (a) *J-V* characteristics and (b) PCE statistics with scan rate of 1 V s<sup>-1</sup>, and (c) PCE variations at different scan rates. HTL-free-PSCs: (d) *J-V* characteristics and (e) PCE statistics with scan rate of 1 V s<sup>-1</sup>, and (f) PCE variations at different scan rates. Tri-layer-PSCs: (g) *J-V* characteristics with a scan rate of 1 V s<sup>-1</sup> and (h) PCE statistics with scan rate of 1 V s<sup>-1</sup>, and (i) PCE variations at different scan rates. 10 devices for each measured group in Figures 1b, 1c, 1e, 1f, 1h, and 1i.

Next, the spiro-OMeTAD layer and Au electrode were replaced by the low-cost carbon electrode for realizing the HTL-free-PSC (Table 1). The *J-V* curves and corresponding photovoltaic parameters of these HTL-free-PSCs are presented in Figure 1d and Table

S2, respectively. The stoichiometric ratio based HTL-free-PSC showed an overall PCE of 16.3%, with a  $V_{oc}$  of 1.08 V,  $J_{sc}$  of 23.51 mA cm<sup>-2</sup>, and FF of 0.642. The average PCEs of the HTL-free-PSCs exhibited similar evolution as that of the full-PSC, as shown in Figure 1e. Unlike the full-PSCs, without the blocking effect of ion migration from the HTL layer, the PCEs of all five groups of HTL-free-PSCs showed a noticeable downward trend as the scan rate decreased from 2 V s<sup>-1</sup> to 0.05 V s<sup>-1</sup> (Figure 1f). The PCE variation of the 1.00 based HTL-free-PSCs when measured at different scan rates was smallest among the five groups, reflecting that the ion migration was reduced within the 1.00 film, which is in accordance with recent results that the degree of ion migration varies within the MAPbI<sub>3</sub> samples fabricated with different precursor ratios.<sup>40-43</sup> These results are consistent with the forward (FW) and backward (BW) scans hysteresis results (Table S2) in the J-V measurements for various PSCs.

Table 1. Cost of fabricating functional layers within PSCs.

Raw materials		Amount	Unit Price (\$)
Substrate	FTO/glass	1 m <sup>2</sup>	228.2
ETL	$SnO_2$	1 mL	6.8
Perovskite	$PbI_2$	1 g	3.6
	MAI	1 g	7.6
	PFTeDA	1 g	16.0
HTL	Spiro-OMeTAD	1 g	478.1

	4-tert-butylpyridine	1 g	5.6
	Li salt	1 g	6.5
Back electrode	Au	1 g	84.0
	Carbon	1 g	0.12

Note: 1) the solvents for preparing perovskite precursor solution (DMF and DMSO) and antisolvent (chlorobenzene, also for HTL solution preparing) have been omitted; 2) the thermal evaporation deposition of the Au electrode is expensive due to the requirement of high vacuum and melting of Au at high temperature; 3) the spin-coating of HTL will increase the cost as well.

Lastly, the SnO<sub>2</sub> ETL was removed from the system to fabricate a simplified tri-layer-PSC. The PCE for the tri-layer-PSC increased from 6.1% of the 0.94 device to 7.7% of the 0.96 device and further reached 9.9% of the 1.00 device. The PCE then decreased to 8.5% of 1.03 device and further reduced to 6.7% for the 1.06 device, as illustrated in Figures 1g, 1h and Table S3. The IPCE spectra of the 0.94, 1.00, and 1.06 based tri-layer-PSCs are shown in Figure S2. The integrated current values were 22.21, 22.42, and 22.03 mA cm<sup>-2</sup> for these devices, which agreed closely with the  $J_{sc}$  values extracted from J-V curves. As compared Figure 1g with Figures 1a and 1d, the  $V_{oc}$  variations of tri-layer-PSC was significant, indicating that strong ion migration in 0.94, 0.97, 1.03, and 1.06 samples would reduce  $V_{oc}$ .<sup>42</sup> Without both ETL and HTL, the PCE variations among the five groups of tri-layer-PSCs were significantly amplified, as shown in Figure 1i. As for the 0.94 based tri-layer-PSCs, the average PCE measured with scan

rate of  $0.05~\rm V~s^{-1}$  was only 21.5% of the average PCE measured with scan rate of  $2~\rm V~s^{-1}$ . This value was 34.3%, 65.8%, 59.4%, and 40.0% for the 0.97, 1.00, 1.03, and 1.06 based tri-layer-PSCs, respectively.

To figure out the origin of the PCE variations among the CTL-free-PSCs, X-ray diffraction (XRD, Figure S3), optical absorption (Figure S4), and X-ray photoelectron spectroscopy (XPS, Figure S5) measurements were performed. These results clearly indicated that the remarkable PCE variations within the CTL-free-PSCs (Figures 1d and 1g) and measured PCE differences at different scan rates (Figures 1f and 1i) originated from the strong ion migration (Note S1).<sup>32,42</sup>

The ion migration within the MAPbI<sub>3</sub> film can be accelerated by applying external voltage bias. A0,43 Here, a voltage of 3.2 V was applied on the perovskite films for 12 h (Figure S6) to accelerate the ion migration within the samples. Multiple characterizations were conducted to document the variations in terms of morphology (scanning electron microscopy, SEM), optical absorption (optical absorption spectroscopy), crystal structural and composition (XRD), and surface potential (Kelvin probe force microscopy, KPFM) of these perovskite samples. Figure S7 shows the SEM images of the 0.94, 1.00, and 1.06 samples before and after the 12 h of external voltage bias. Rougher surfaces could be observed within all three perovskite films after 12 h of 3.2 V bias, indicating that the accelerated ion migration under external voltage bias could even change the surface morphology of the samples. The bright features in the

0.94 and 1.06 perovskite films (Figures S7d and S7f) indicated that more PbI<sub>2</sub> might be generated within these films after 12 h of 3.2 V bias as compared to 1.00 sample (Figure S7e). The generation of PbI<sub>2</sub> within the 0.94 and 1.06 perovskite films was documented with optical absorption spectroscopy, as shown in Figures S8a and S8c. However, the optical absorption feature of PbI<sub>2</sub> within the 1.00 perovskite film was not significant (Figure S8b). XRD measurements were performed to check the differences in crystal structural before and after the 12 h of 3.2 V bias, as shown in Figures 2a-2c. The XRD peak intensity of PbI<sub>2</sub> for the 0.94 and 1.06 samples was significantly enhanced as compared to the 1.00 sample, so the external voltage bias driven ion migration would result in more PbI<sub>2</sub> left within the 0.94 and 0.96 films as compared to the 1.00 film. KPFM measurements (Note S2) were conducted to check the surface Fermi level differences after the 12 h of 3.2 V bias, as shown in Figures 2d-2l. Pristine perovskite films showed n-type nature and the estimated Fermi levels were -4.40 eV, -4.42 eV, and -4.45 eV for the 0.94, 1.00, and 1.06 samples, respectively (Figures 2j-21 and Table S4). After the 12 h of 3.2 V bias, the Fermi levels were lifted up to -4.02 eV, -4.06 eV, and -3.98 eV for the 0.94, 1.00, and 1.06 eV, respectively (Figures 2j-21 and Table S4), reflecting that the surface regions within these perovskite films were more n doped and the surface composition of the perovskite samples was dramatically changed (more PbI<sub>2</sub> exposed at the surface) due to the accelerated ion migration under external voltage bias. 40,44,45 This behavior was noticeable even in the 1.00 sample (Fermi level change from -4.42 eV to -4.06 eV), reflecting that the ion migration can be observed in all the perovskite films. Since the ion migration in the perovskite films exhibited a strong

influence on the device performance, so the performance of the HTL-free-PSCs and trilayer-PSCs can be further improved by suppressing the ion migration within the 1.00 sample (referred as control in the following discussion).

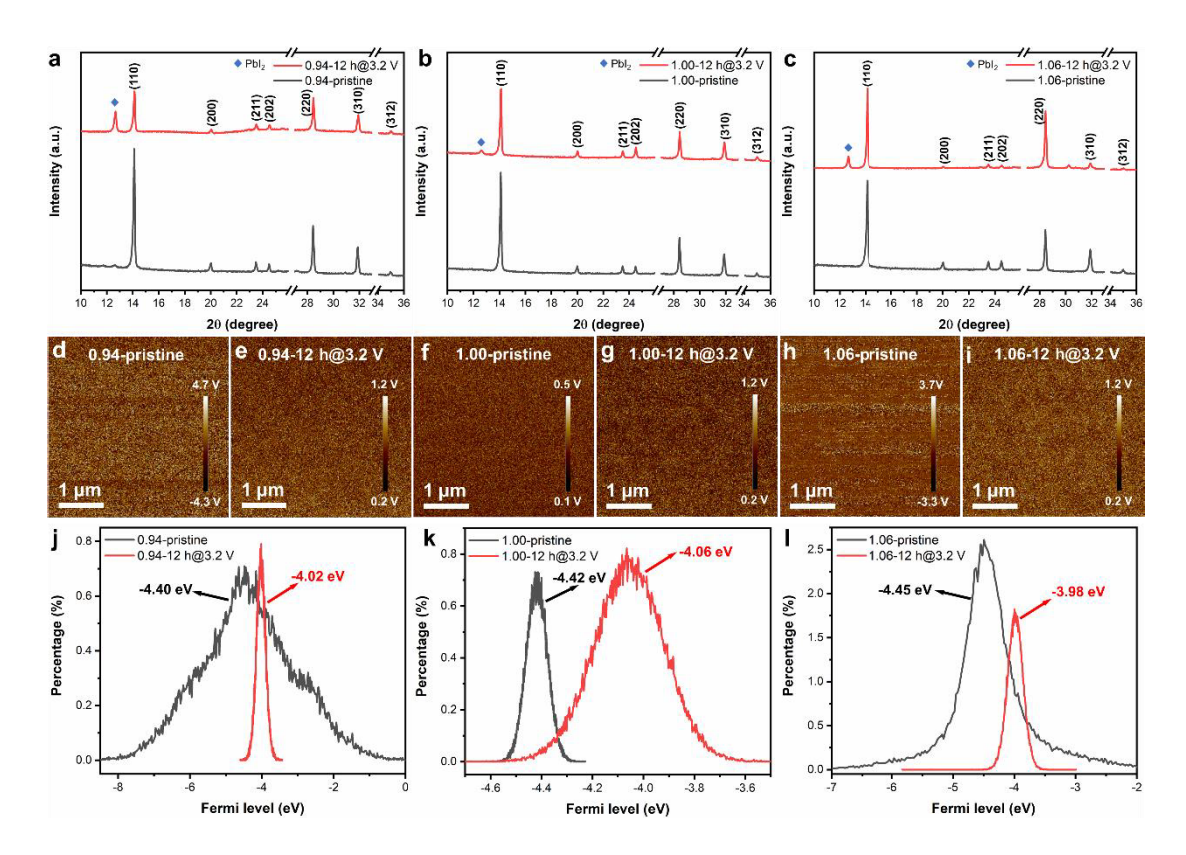


Figure 2. Ion migration within different perovskite films. XRD patterns of the (a) 0.94, (b) 1.00, and (c) 1.06 films before and after 12 h of 3.2 V bias. Surface potential mapping features measured by KPFM for 0.94 (d, e), 1.00 (f, g), and 1.06 (h, i) films before (d, f, h) and after 12 h of 3.2 V bias (e, g, i). Fermi level profiles of the (j) 0.94, (k) 1.00, and (l) 1.06 films before and after 12 h of 3.2 V bias.

To further suppress the ion migration within the HTL-free-PSCs and tri-layer-PSC, PFTeDA with 27 fluorine atoms and a carbonyl unit was introduced as an additive in the system (referred as target in the following text). Organic molecules with carbonyl

units have been introduced into the MAPbI<sub>3</sub> system for efficient ion migration suppression and defect passivation since they will locate at surface and grain boundaries due to the chelation between noncoordinating lead and carbonyl unit. 46,47 The carbon fluorine bonds exhibit highly hydrophobic chemical properties which induce kinetic barriers that slow the ion migration of  $MA^+/I^-$  and intrusion of  $O_2$  and  $H_2O.^{46,48,49}$  Thus, in this study, the incorporation of PFTeDA is designed for efficiently blocking the ion migration, passivating crystal defects, and enhancing overall device stability in the MAPbI<sub>3</sub>-based CTL-free-PSCs. The cross-section SEM image of a HTL-free-PSC can be found in Figure 3a, the perovskite film was compactly coated on the FTO/SnO<sub>2</sub> substrate and the carbon electrode was densely deposited on top of the perovskite light absorber. The PCE of the HTL-free-PSC increased from 16.3% of the control device to 18.9% of the target device (with  $V_{oc}$  of 1.10 V,  $J_{sc}$  of 23.85 mA cm<sup>-2</sup>, FF of 0.718), which is a record efficiency for the carbon-based HTL-free-PSC (Figure 3b and Table S5). Figure 3c exhibits that the average PCE of the target HTL-free-PSCs measured at a scan rate of 0.05 V s<sup>-1</sup> was similar with that measured at a scan rate of 2 V s<sup>-1</sup>, indicating that the PCE variation of the target HTL-free-PSCs was much reduced as compared to the control device. The stability of the HTL-free-PSCs were investigated in ambient air conditions for over 1 year. The unencapsulated control devices maintained 78.4% of their initial PCE after 366 days of storage under ambient air conditions (~40% relative humidity) at RT, while the target device retained 92.4% of their initial PCE during the same period under similar conditions, as illustrated in Figure 3d (10 devices for each group). These results were in accordance with the water contact angle results, as shown

in Figure S9, which suggests that the PFTeDA addition increases the water contact angle from 40.2 degree of the control sample to 71.2 degree of the target sample. Furthermore, the incorporation of PFTeDA also enhanced the device performance (PCE and various stabilities) of the tri-layer-PSCs, as illustrated in Figures S10-S15, Table S5 and Note S3.<sup>50,51</sup>

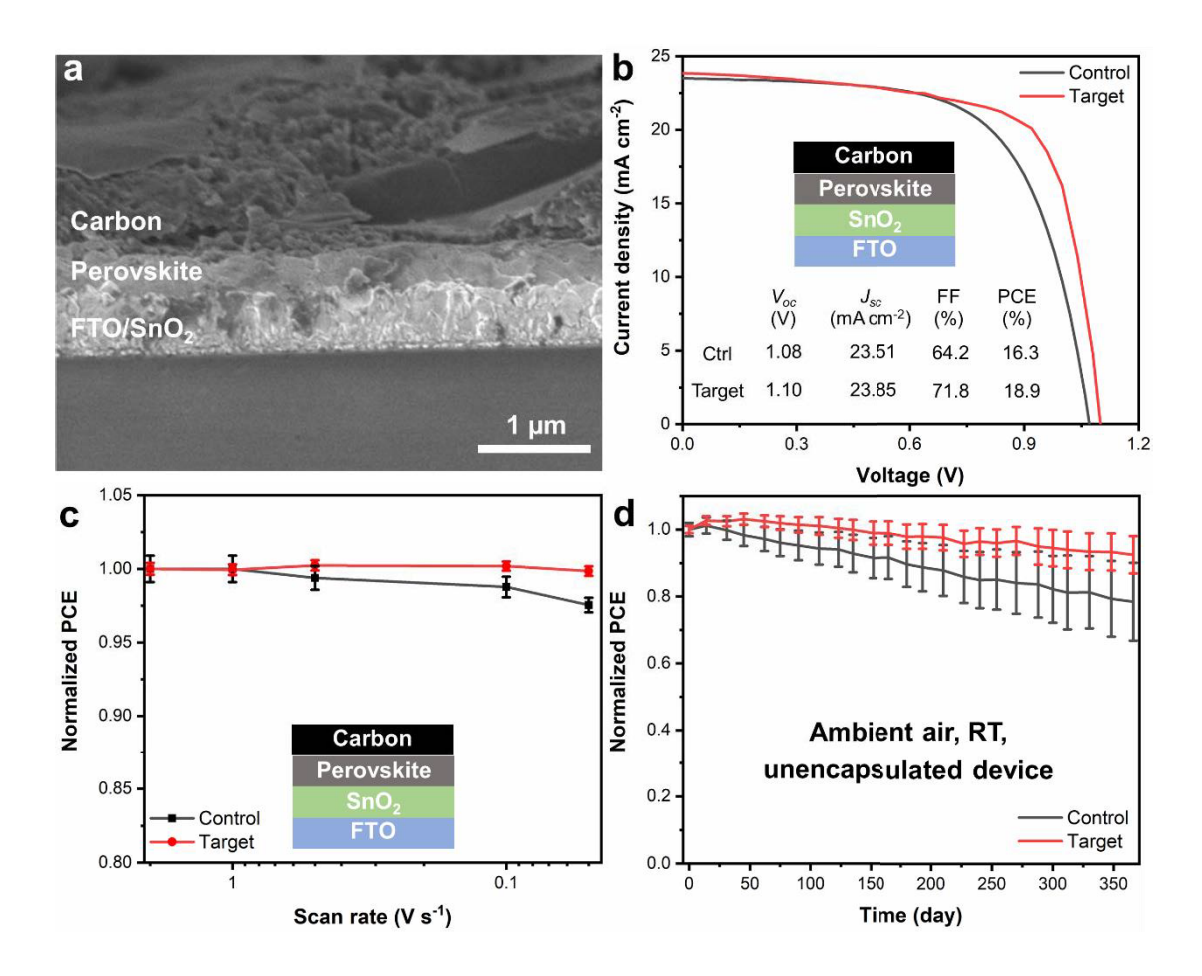
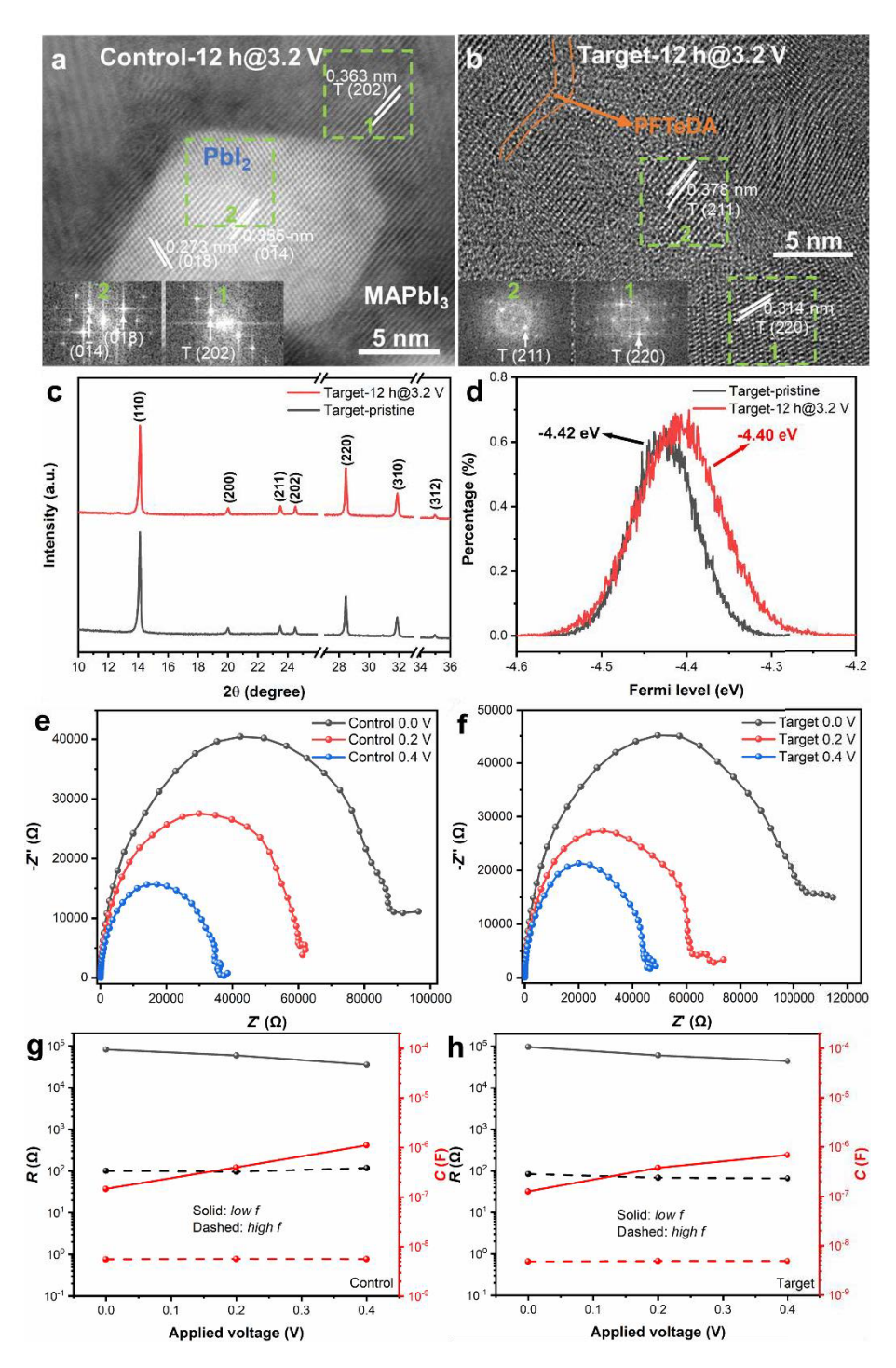


Figure 3. HTL-free-PSC performance enhancement with PFTeDA additive. (a) Cross-section SEM images for a HTL-free-PSC. (b) *J-V* characteristics determined under simulated 1 Sun illumination with a scan rate of 1 V s<sup>-1</sup> for the control and target devices. (c) PCE variations measured at different scan rates for the control and target HTL-free-PSCs (10 devices for each group). (d) Stability measurements of the

unencapsulated control and target HTL-free-PSCs under ambient air at RT.

The material property changes after the incorporation of PFTeDA have been investigated (Figures S16-S18, Note S4, and Tables S6 and S7). The PFTeDA formed an amorphous thin layer between adjacent perovskite crystals. After the incorporation of the PFTeDA, the decreased crystal defect density and enhanced charge carrier mobility could be obtained in the target sample, leading to the PCE improvement of the target CTL-free-PSCs. 52,53 To further understand the detailed ion migration suppression mechanisms driving the PCE and overall stability enhancements of CTL-free-PSCs with the modification of PFTeDA, systematic characterizations were performed on the perovskite samples. The crystal structure details of both control and target samples after 12 h of 3.2 V bias are presented in Figures 4a and 4b. Figure 4a indicates that PbI<sub>2</sub> (Table S8) was formed after the 12 h of external voltage bias, which is accordance with the XRD results (Figure 2b). However, the target sample maintained the tetragonal nature during the same period under the similar conditions. Similarly, the differences, including crystal structure (XRD results in Figure 4c) Fermi level (KPFM results in Figures 4d and S19, and Table S4), optical absorption (Figure S20), and morphology (SEM images in Figure S21), of the target samples before and after 12 h of 3.2 V bias were much smaller than those of the control samples under the same voltage bias (Figures 2b, 2f, 2g, 2k, S7b, S7e, and S8b). Thus, the incorporation of PFTeDA within the system would block the ion migration thereafter increase the stability of the perovskite crystal.



**Figure 4. Suppression of ion migration within perovskite after the incorporation of PFTeDA**. TEM results of (**a**) control and (**b**) target films after 12 h of 3.2 V bias. Insets No. 1 and 2 in (**a**) show the FFT patterns of tetragonal MAPbI<sub>3</sub> and PbI<sub>2</sub> for the green dotted line circled areas 1 and 2, respectively. Insets No. 1 and 2 in (**b**) show the

FFT patterns of tetragonal MAPbI<sub>3</sub> for the green dotted line circled areas 1 and 2, respectively. The orange dotted line circled area of (**b**) indicates the existence of the PFTeDA amorphous thin layer at the perovskite crystal boundaries. Capitals T letters in (**a** and **b**) are included in front of the planes and directions to denote the tetragonal (T) MAPbI<sub>3</sub> phase indices. (**c**) XRD patterns and (**d**) Fermi level profiles of the target film before and after 12 h of 3.2 V bias. Nyquist plots of (**e**) control and (**f**) target PSCs measured at different applied voltages under dark conditions. Resistance and capacitance results of (**g**) control and (**h**) target PSCs obtained by describing the EIS data measured in (**e**) and (**f**).

Electrochemical impedance spectroscopy (EIS) measurements<sup>54-56</sup> were conducted to quantify the charge transport, recombination dynamics, and ion migration within the tri-layer-PSCs. Figures 4e and 4f show the Nyquist plots of both control and target devices measured under the ambient air dark conditions with different applied voltages. The plots of the real part of the impedances and the real part of the capacitances can be found in Figures S22 and S23, respectively. These parameters are summarized in Figures 4g and 4h. The values of the real part of impedances (low f, related to recombination resistance) of the target device were larger than that of the control device, which means that the defect passivation through PFTeDA modification can successfully suppress the non-radiative charge carrier recombination. The high f capacitance is the classical electrostatic capacitance produced by the electrical field between two plates. In contrast, the low f capacitance reflects the capability of a system to accept or release

additional carriers due to a change in their chemical potential. The corresponding low f capacitances were gradually increased for both control and target devices as the applied voltage increase, but the low f capacitances of the target device were always smaller than that of the control device at 0 V (1.25  $\times$  10<sup>-7</sup> F vs. 1.47 $\times$  10<sup>-7</sup> F), 0.2 V (3.78  $\times$  10<sup>-7</sup>  $^{7}$  F vs.  $3.99 \times 10^{-7}$  F), and 0.4 V ( $6.89 \times 10^{-7}$  F vs.  $1.12 \times 10^{-6}$  F), indicating that more free carriers were collected within the PFTeDA modified device. The time constants extracted from EIS data for both control and target devices are plotted in Figure S24 as a function of the applied voltage. According to recently reported results, 55,57 the low f time constants-bias voltage relation provides the information on ion migration. A smaller low f time constants variation was calculated for the target device (12.1 ms at 0 V to 30.4 ms at 0.4 V) as compared to the control sample (12.0 ms at 0 V to 39.4 ms at 0.4 V), indicating that the ion migration within the target device was suppressed after the incorporation of PFTeDA. These results are consistent with the temperaturedependent dark conductivity measurements that the extracted activation energy of the PFTeDA modified sample is larger than that of the control sample, as shown in Figure S25.58,59

Results reported here demonstrate the facile construction of efficient CTL-free-PSCs by suppressing ion migration and passivating crystal defects through the PFTeDA additive. Detailed systematic analysis conducted on perovskite material and various device configurations indicate that the ion migration in control sample led to remarkable PCE variations when the CTL-free-PSCs were measured at different scan

rates. After the incorporation of the PFTeDA, ion migration and crystal defects were significantly reduced within the target film. The PFTeDA modified CTL-free-PSCs exhibited much improved PCE and decreased PCE variation when they were measured at different scan rates. The incorporation of PFTeDA further increased the stability of the perovskite crystals, resulting in enhanced environmental, thermal, and light stabilities for the CTL-free-PSCs. These results provide a transformative solution for the realization of highly efficient, stable, and low-cost CTL-free solar cell.

## **Supporting Information**

The Supporting Information is available free of charge on the ACS Publications website at xx. Experimental section, IPCE, XRD, optical absorption, XPS, images, SEM, water contact angle, *J-V*, device stabilities, schematic, KPFM, EIS, TRPL, FTIR, temperature-dependent ionic conductivity, simulated crystal results.

#### **Author Information**

\*Corresponding author. Email: <a href="mailto:tvy5161@psu.edu">tvy5161@psu.edu</a>; kaiwang@psu.edu; sup103@psu.edu.

#### **Notes**

The authors declare no competing financial interests.

## **ACKNOWLEDGMENTS**

This material is based upon work supported by the U.S. Department of Energy Award No. DE-SC0019844, under the STTR program (Prime - NanoSonic Inc.), T.Y. and J.Y. acknowledge the support from this project. Co-authors K.W. and Y.H. acknowledge the

support from Air Force Office of Scientific Research BioPhysics program (award number FA9550-20-0157). S.P. acknowledges the support from National Science Foundation through award number 1936432. A.N. acknowledges the support through Office of Naval Research award number N00014-20-1-2602. L.Z. acknowledges the support through National Science Foundation I/UCRC: Center for Energy Harvesting Materials and Systems. D.Y. acknowledges the support from the Norfolk State University through NSF CREST program.

#### DISCLAIMER

This report was prepared as an account of work sponsored by an agency of the United States Government. Neither the United States Government nor any agency thereof, nor any of their employees, makes any warranty, express or implied, or assumes any legal liability or responsibility for the accuracy, completeness, or usefulness of any information, apparatus, product, or process disclosed, or represents that its use would not infringe privately owned rights. Reference herein to any specific commercial product, process, or service by trade name, trademark, manufacturer, or otherwise does not necessarily constitute or imply its endorsement, recommendation, or favoring by the United States Government or any agency thereof. The views and opinions of authors expressed herein do not necessarily state or reflect those of the United States Government or any agency thereof.

## References

1. Jeon, N. J., Noh, J. H., Yang, W. S., Kim, Y. C., Ryu, S., Seo, J., Seok, S. I.

- Compositional engineering of perovskite materials for high-performance solar cells. *Nature* **2015**, *517*, 476-480.
- Saliba, M., Matsui, T., Seo, J. Y., Domanski, K., Correa-Baena, J. P., Nazeeruddin, M. K., Zakeeruddin, S. M., Tress, W., Abate, A., Hagfeldt, A., Grätzel, M. Cesium-containing triple cation perovskite solar cells: improved stability, reproducibility and high efficiency. *Energy Environ. Sci.* 2016, 9, 1989-1997.
- Mei, A., Sheng, Y., Ming, Y., Hu, Y., Rong, Y., Zhang, W., Luo, S., Na, G., Tian,
   C., Hou, X., Xiong, Y., Zhang, Z., Liu, S., Uchida, S., Kim, T.-W., Yuan, Y.,
   Zhang, L., Zhou, Y., Han, H. Stabilizing perovskite solar cells to IEC61215: 2016
   standards with over 9,000-h operational tracking. *Joule* 2020, 4, 2646-2660.
- Bi, D., Yi, C., Luo, J., Décoppet, J. D., Zhang, F., Zakeeruddin, S. M., Li, X., Hagfeldt, A., Grätzel, M. Polymer-templated nucleation and crystal growth of perovskite films for solar cells with efficiency greater than 21%. *Nat. Energy* 2016, 1, 16142.
- Mei, A., Li, X., Liu, L., Ku, Z., Liu, T., Rong, Y., Xu, M., Hu, M., Chen, J., Yang,
   Y., Grätzel, M., Han, H. A hole-conductor-free, fully printable mesoscopic perovskite solar cell with high stability. *Science* 2014, 345, 295-298.
- Shin, S. S., Yeom, E. J., Yang, W. S., Hur, S., Kim, M. G., Im, J., Seo, J., Noh, J.
   H., Seok, S. I. Colloidally prepared La-doped BaSnO<sub>3</sub> electrodes for efficient, photostable perovskite solar cells. *Science* 2017, 356, 167-171.
- 7. Kojima, A., Teshima, K., Shirai, Y., Miyasaka, T. Organometal Halide Perovskites as Visible-Light Sensitizers for Photovoltaic Cells. *J. Am. Chem. Soc.* **2017**, *131*,

6050-6051.

- 8. Kim, H. -S., Lee, C. -R., Im, J. -H., Lee, K. -B., Moehl, T., Marchioro, A., Moon, S. -J., Humphry-Baker, R., Yum, J. -H., Moser, J. E., Grätzel, M., Park, N. -G. Lead iodide perovskite sensitized all-solid-state submicron thin film mesoscopic solar cell with efficiency exceeding 9%. *Sci. Rep.* **2012**, *2*, 591.
- 9. Lee, M. M., Teuscher, J., Miyasaka, T., Murakami, T. N., Snaith, H. J. Efficient hybrid solar cells based on meso-superstructured organometal halide perovskites. *Science* **2012**, *338*, 643-647.
- Jiang, Q., Zhao, Y., Zhang, X., Yang, X., Chen, Y., Chu, Z., Ye, Q., Li, X., Yin,
   Z., You, J. Surface passivation of perovskite film for efficient solar cells. *Nat. Photon.* 2019, 13, 460-466.
- Wang, K., Wu, C., Hou, Y., Yang, D., Ye, T., Yoon, J., Sanghadasa, M., Priya, S.
   Isothermally crystallized perovskites at room-temperature. *Energy Environ. Sci.* 2020, 13, 3412-3422.
- 12. Jang, Y. W., Lee, S., Yeom, K. M., Jeong, K., Choi, K., Choi, M., Noh, J. H. Intact 2D/3D halide junction perovskite solar cells via solid-phase in-plane growth. *Nat. Energy* **2021**, *6*, 63-71.
- 13. National Renewable Energy Laboratory. *Best Research-Cell Efficiency Chart*. <a href="https://www.nrel.gov/pv/cell-efficiency.html">https://www.nrel.gov/pv/cell-efficiency.html</a> (accessed 2021-06-04).
- 14. Wu, W. Q., Chen, D., Caruso, R. A., Cheng, Y. B. Recent progress in hybrid perovskite solar cells based on n-type materials. *J. Mater. Chem. A* 2017, 5, 10092-10109.

- 15. Wu W. Q., Wang, L. 3D Branched nanowire-coated macroporous titania thin films for efficient perovskite solar cells. *Adv. Funct. Mater.* **2018**, *28*, 1804356.
- 16. Li, Y., Ye, S., Sun, W., Yan, W., Li, Y., Bian, Z., Liu, Z., Wang, S., Huang, C. Holeconductor-free planar perovskite solar cells with 16.0% efficiency. *J. Mater. Chem.*A 2015, 3, 18389-18394.
- 17. Liao, J. F., Wu, W. Q., Jiang, Y., Zhong, J. X., Wang, L., Kuang, D. B. Understanding of carrier dynamics, heterojunction merits and device physics: towards designing efficient carrier transport layer-free perovskite solar cells. *Chem. Soc. Rev.* 2020, 49, 354-381.
- 18. Sutherland, B. R., Sargent, E. H. Perovskite photonic sources. *Nat. Photonics* **2020**, *10*, 295-302.
- 19. Ye, T., Ma, S., Jiang, X., Wei, L., Vijila, C., Ramakrishna, S. Performance enhancement of tri-cation and dual-anion mixed perovskite solar cells by Au@SiO<sub>2</sub> nanoparticles. *Adv. Funct. Mater.* **2017**, *27*, 1606545.
- 20. Zhang, Z., Fang, W. H., Long, R., Prezhdo, O. V. Exciton dissociation and suppressed charge recombination at 2D perovskite edges: key roles of unsaturated halide bonds and thermal disorder. *J. Am. Chem. Soc.* **2017**, *141*, 15557-15566.
- 21. Ye, T., Petrović, M., Peng, S., Yoong, J. L. K., Vijila, C., Ramakrishna, S. Enhanced charge carrier transport and device performance through dual-cesium doping in mixed-cation perovskite solar cells with near unity free carrier ratios. ACS Appl. Mater. Interfaces 2017, 9, 2358-2368.
- 22. Li, F., Ma, C., Wang, H., Hu, W., Yu, W., Sheikh, A. D., Wu, T. Ambipolar solution-

- processed hybrid perovskite phototransistors. Nat. Commun. 2015, 6, 8238.
- 23. Wei, Z., Yan, K., Chen, H., Yi, Y., Zhang, T., Long, X., Li, J., Zhang, L., Wang, J., Yang, S. Cost-efficient clamping solar cells using candle soot for hole extraction from ambipolar perovskites. *Energy Environ. Sci.* 2014, 7, 3326-3333.
- 24. Dong, Q., Fang, Y., Shao, Y., Mulligan, P., Qiu, J., Cao, L., Huang, J. Electron-hole diffusion lengths > 175 μm in solution-grown CH<sub>3</sub>NH<sub>3</sub>PbI<sub>3</sub> single crystals. *Science* 2015, 347, 967-970.
- 25. Petrović, M., Ye, T., Vijila, C., Ramakrishna, S. Influence of charge transport and defects on the performance of planar and mesostructured perovskite solar cells, *Adv. Energy Mater.* **2017**, *7*, 1602610.
- 26. Tan, H., Che, F., Wei, M., Zhao, Y., Saidaminov, M.I., Todorović, P., Broberg, D., Walters, G., Tan, F., Zhuang, T., Sun, B., Liang, Z., Yuan, H., Fron, E., Kim, J., Yang, Z., Voznyy, O., Asta, M., Sargent, E. H. Dipolar cations confer defect tolerance in wide-bandgap metal halide perovskites. *Nat. Commun.* 2018, 9, 3100.
- 27. Meggiolaro, D., Motti, S. G., Mosconi, E., Barker, A. J., Ball, J., Perini, C. A. R., Deschler, F., Petrozza, A., De Angelis, F. Iodine chemistry determines the defect tolerance of lead-halide perovskites. *Energy Environ. Sci.* 2018, *11*, 702-713.
- 28. Chen, Z., Wang, J.J., Ren, Y., Yu, C., Shum, K. Schottky Solar Cells Based on CsSnI<sub>3</sub> Thin-Films. *Appl. Phys. Lett.* **2012**, *101*, 093901.
- 29. Xu, X., Liu, Z., Zuo, Z., Zhang, M., Zhao, Z., Shen, Y., Zhou, H., Chen, Q., Yang, Y., Wang, M. Hole selective NiO contact for efficient perovskite solar cells with carbon electrode. *Nano Lett.* **2015**, *15*, 2402-2408.

- 30. Hu, Y., Zhang, Z., Mei, A., Jiang, Y., Hou, X., Wang, Q., Du, K., Rong, Y., Zhou, Y., Xu, G, Han, H. Improved performance of printable perovskite solar cells with bifunctional conjugated organic molecule. *Adv. Mater.* **2018**, *30*, 1705786.
- 31. Sun, H., Deng, K., Xiong, J., Li, L. Graded Bandgap Perovskite with Intrinsic n–p

  Homojunction Expands Photon Harvesting Range and Enables All Transport

  Layer-Free Perovskite Solar Cells. *Adv. Energy Mater.* **2020**, *10*, 1903347.
- 32. Dong, Q., Song, J., Fang, Y., Shao, Y., Ducharme, S., Huang, J. Lateral-structure single-crystal hybrid perovskite solar cells via piezoelectric poling. *Adv. Mater.* **2016**, *28*, 2816-2821.
- 33. Zhou, Q., Duan, J., Yang, X., Duan, Y., Tang, Q. Interfacial strain release from the WS<sub>2</sub>/CsPbBr<sub>3</sub> van der Waals heterostructure for 1.7 V voltage all-inorganic perovskite solar cells. *Angew. Chem. Int. Ed.* **2020**, *132*, 22181-22185.
- 34. Huang, L., and Ge, Z. Simple, Robust, Going More Efficient: Recent Advance on Electron Transport Layer-Free Perovskite Solar Cells. *Adv. Energy Mater.* **2019**, *9*, 1900248.
- 35. Aitola, K., Domanski, K., Correa-Baena, J.P., Sveinbjörnsson, K., Saliba, M., Abate, A., Grätzel, M., Kauppinen, E., Johansson, E.M., Tress, W., Hagfeldt, A., Boschloo, G. High temperature-stable perovskite solar cell based on low-cost carbon nanotube hole contact. *Adv. Mater.* **2019**, *29*, 1606398.
- 36. Planes, E., Perrin, L., Matheron, M., Spalla, M., Berson, S., Flandin, L. Degradation mechanisms in a mixed cations and anions perovskite solar cell: mitigation effect of the gold electrode. *ACS Appl. Energy Mater.* **2021**, *4*, 1365-

- 37. Wei, Z., Chen, H., Yan, K., Yang, S. Inkjet printing and instant chemical transformation of a CH<sub>3</sub>NH<sub>3</sub>PbI<sub>3</sub>/nanocarbon electrode and interface for planar perovskite solar cells. *Angew. Chem. Int. Ed.* **2014**, *53*, 13239-13243.
- 38. Wu, C., Wang, K., Jiang, Y., Yang, D., Hou, Y., Ye, T., Han, C. S., Chi, B., Zhao, L., Wang, S., Deng, W., Priya, S. All Electrospray Printing of Carbon-Based Cost-Effective Perovskite Solar Cells. *Adv. Funct. Mater.* **2021**, *31*, 2006803.
- 39. Zhang, H., Xiao, J., Shi, J., Su, H., Luo, Y., Li, D., Wu, H., Cheng, Y. B., Meng, Q. Self-adhesive macroporous carbon electrodes for efficient and stable perovskite solar cells. *Adv. Funct. Mater.* **2018**, *28*, 1802985.
- 40. Yuan, Y., Huang, J. Ion migration in organometal trihalide perovskite and its impact on photovoltaic efficiency and stability. *Acc. Chem. Res.* **2016**, *49*, 286-293.
- 41. Haque, F., Hoang, N.T.T., Ji, J., Mativenga, M. Effect of precursor composition on ion migration in hybrid perovskite CH<sub>3</sub>NH<sub>3</sub>PbI<sub>3</sub>. *IEEE Electron Device Lett.* **2019**, 40, 1756-1759.
- 42. Zhao, Y., Zhou, W., Han, Z., Yu, D., Zhao, Q. Effects of ion migration and improvement strategies for the operational stability of perovskite solar cells. *Phys. Chem. Chem. Phys.* **2021**, *23*, 94-106.
- 43. Huang, S., Shi, L., Zou, T., Kuang, H., Rajagopalan, P., Xu, H., Zhan, S., Chen, J., Xuan, W., Jin, H., Dong, S., Zhou, H., Wang, X., Yin, W., Kim, J. M., Luo, J. Controlling performance of organic-inorganic hybrid perovskite triboelectric nanogenerators via chemical composition modulation and electric field-induced

- ion migration. Adv. Energy Mater. 2020, 10, 2002470.
- 44. Wang, Q., Shao, Y., Xie, H., Lyu, L., Liu, X., Gao, Y., Huang, J. Qualifying composition dependent p and n self-doping in CH<sub>3</sub>NH<sub>3</sub>PbI<sub>3</sub>. *Appl. Phys. Lett.* **2014**, *105*, 163508.
- 45. Cui, P., Wei, D., Ji, J., Huang, H., Jia, E., Dou, S., Wang, T., Wang, W., Li, M. Planar p–n homojunction perovskite solar cells with efficiency exceeding 21.3%. *Nat. Energy* **2019**, *4*, 150-159.
- 46. Yang, J., Liu, C., Cai, C., Hu, X., Huang, Z., Duan, X., Meng, X., Yuan, Z., Tan, L., Chen, Y. High-performance perovskite solar cells with excellent humidity and thermo-stability via fluorinated perylenediimide. *Adv. Energy Mater.* 2019, 9, 1900198.
- 47. Wang, Y., Chao, L., Niu, T., Li, D., Wei, Q., Wu, H., Qiu, J., Lu, H., Ran, C., Zhong, Q., Song, L., Xing, G., Xia, Y., Chen, Y., Müller-Buschbaum, P., Huang, W. Efficient and stable perovskite solar cells by fluorinated ionic liquid-induced component interaction. *Solar RRL* 2021, 5, 2000582.
- 48. Zhu, H., Ren, Y., Pan, L., Ouellette, O., Eickemeyer, F. T., Wu, Y., Li, X., Wang, S., Liu, H., Dong, X., Zakeeruddin, S. M., Liu, Y., Hagfeldt, A., Grätzel, M. Synergistic effect of fluorinated passivator and hole transport dopant enables stable perovskite solar cells with an efficiency near 24%. *J. Am. Chem. Soc.* 2021, 143, 3231-3237.
- 49. Jeong, M., Choi, I. W., Go, E. M., Cho, Y., Kim, M., Lee, B., Jeong, S., Jo, Y., Choi, H. W., Lee, J., Bae, J. H., Kwak, S. K., Kim, D. S., Yang, C. Stable perovskite solar

- cells with efficiency exceeding 24.8% and 0.3-V voltage loss. *Science* **2020**, *369*, 1615-1620.
- 50. Habisreutinger, S. N., Noel, N. K., Snaith, H. J. Hysteresis index: A figure without merit for quantifying hysteresis in perovskite solar cells. *ACS Energy Lett.* **2018**, *3*, 2472-2476.
- 51. Ye, T., Wang, K., Ma, S., Wu, C., Hou, Y., Yang, D., Wang, K., Priya, S. Strain-relaxed tetragonal MAPbI<sub>3</sub> results in efficient mesoporous solar cells. *Nano Energy* **2021**, *83*, 105788.
- 52. Zhou, Y., Yin, Y., Zuo, X., Wang, L., Li, T.D., Zhou, Y., Padture, N. P., Yang, Z., Guo, Y., Xue, Y., Kisslinger, K., Cotlet, M., Nam, C. Y., Rafailovich M. H. Enhancing chemical stability and suppressing ion migration in CH<sub>3</sub>NH<sub>3</sub>PbI<sub>3</sub> perovskite solar cells via direct backbone attachment of polyesters on grain boundaries. *Chem. Mater.* **2020**, *32*, 5104-5117.
- 53. Ye, T., Bruno, A., Han, G., Koh, T. M., Li, J., Jamaludin, N. F., Soci, C., Mhaisalkar, S. G., Leong, W. L. Efficient and ambient-air-stable solar cell with highly oriented 2D@ 3D perovskites. *Adv. Funct. Mater.* **2018**, *28*, 1801654.
- 54. Ye, T., Wang, K., Hou, Y., Yang, D., Smith, N., Magill, B., Yoon, J., Mudiyanselage, R. R. H. H., Khodaparast, G. A., Wang, K., Priya, S. Ambient-Air-Stable Lead-Free CsSnI<sub>3</sub> Solar Cells with Greater than 7.5% efficiency. *J. Am. Chem. Soc.* **2021**, DOI: 10.1021/jacs.0c13069.
- 55. Ebadi, F., Taghavinia, N., Mohammadpour, R., Hagfeldt, A., Tress, W. Origin of apparent light-enhanced and negative capacitance in perovskite solar cells. *Nat*.

- Commun. 2019, 10, 1574.
- 56. Yoo, S. M., Yoon, S. J., Anta, J. A., Lee, H. J., Boix, P. P., Mora-Seró, I. An equivalent circuit for perovskite solar cell bridging sensitized to thin film architectures. *Joule* **2019**, *3*, 2535-2549.
- Zarazua, I., Han, G., Boix, P. P., Mhaisalkar, S., Fabregat-Santiago, F., Mora-Seró,
   I., Bisquert, J., Garcia-Belmonte, G. Surface recombination and collection efficiency in perovskite solar cells from impedance analysis. *J. Phys. Chem. Lett.* 2016, 7, 5105-5113.
- 58. Tan, S., Yavuz, I., De Marco, N., Huang, T., Lee, S. J., Choi, C. S., Wang, M., Nuryyeva, S., Wang, R., Zhao, Y., Wang, H. C. Steric impediment of ion migration contributes to improved operational stability of perovskite solar cells. *Adv. Mater.* 2020, *32*, 1906995.
- 59. Hong, M., Lyv, W., Li, M., Xu, S., Sun, Q., Zou, J., Chen, Z. G. Rashba effect maximizes thermoelectric performance of GeTe derivatives. *Joule* **2020**, *4*, 2030-2043.